AGU PUBLICATIONS

JGR

Journal of Geophysical Research: Solid Earth

RESEARCH ARTICLE

10.1002/2017JB014926

Key Points:
- A new drag law for nonspherical rough particles is presented
- The drag laws cover all ranges of irregular shapes and fluid dynamic regimes of interest for natural multiphase flows
- The drag law allows to better predict the drag and terminal velocity of irregular particles also at very low *Re*

Supporting Information:
- Supporting Information S1
- Data Set S1
- Data Set S2
- Data Set S3

Correspondence to:
F. Dioguardi,
fabiod@bgs.ac.uk

Citation:
Dioguardi, F., Mele, D., & Dellino, P. (2018). A new one-equation model of fluid drag for irregularly shaped particles valid over a wide range of Reynolds number. *Journal of Geophysical Research: Solid Earth*, *123*, 144–156. https://doi.org/10.1002/2017JB014926

Received 30 AUG 2017
Accepted 8 DEC 2017
Accepted article online 13 DEC 2017
Published online 11 JAN 2018

©2017. British Geological Survey, a component institute of NERC. All Rights Reserved.

A New One-Equation Model of Fluid Drag for Irregularly Shaped Particles Valid Over a Wide Range of Reynolds Number

F. Dioguardi[1], D. Mele[2], and P. Dellino[2]

[1]British Geological Survey, The Lyell Centre, Edinburgh, UK, [2]Dipartimento di Scienze della Terra e Geoambientali, University of Bari, Bari, Italy

Abstract A new drag law for irregularly shaped particles is presented here. Particles are described by a shape factor that takes into account both sphericity and circularity, which can be measured via the most commonly used image particle analysis techniques. By means of the correlation of the drag coefficient versus the particle Reynolds number and the shape factor, a new drag formula, which is valid over a wide range of Reynolds number (0.03–10,000), is obtained. The new model is able to reproduce the drag coefficient of particles measured in terminal velocity experiments with a smaller scatter compared to other laws commonly used in multiphase flow engineering and volcanology. Furthermore, the new formula uses only one equation, whereas previous models, to insure validity over an ample range, made use of a step function that introduces a discontinuity at the switch of equations. Finally, this drag law works in the whole range of variation, from extremely irregular particles to perfect sphere. A code of the iterative algorithm for the drag coefficient calculation and terminal velocity is included in the supporting information both as a Fortran routine and a Matlab function.

1. Introduction

Aerodynamic drag is an important parameter controlling the transport and settling velocity of solid particles in static and moving fluids (Crowe, 2006). In fact, in a multiphase flow, the fluid-particle drag force F_d is defined as

$$F_d = \frac{1}{2}\rho_f C_d A_p \left|\boldsymbol{v_p} - \boldsymbol{v_f}\right| \left(\boldsymbol{v_p} - \boldsymbol{v_f}\right) \tag{1}$$

where ρ_f is the fluid density, C_d is the particle drag coefficient, A_p is the particle surface area, and $\boldsymbol{v_p}$ and $\boldsymbol{v_f}$ are the particle and fluid velocity, respectively (see Table 1 for notation).

Furthermore, a particle falling in a static fluid eventually reaches a constant settling velocity, known as terminal velocity w_t, which is calculated by means of the well-known Newton's impact formula (Dellino et al., 2005):

$$w_t = \sqrt{\frac{4gd_p\left(\rho_p - \rho_f\right)}{3C_d\rho_f}} \tag{2}$$

where g is the gravitational acceleration, d_p is particle size, and ρ_p and ρ_f are the particle and fluid density, respectively. If particles are spherical, well-established relationships linking C_d with the particle Reynolds number *Re* exist, each having a different accuracy and range of applicability (e.g., Clift & Gauvin, 1971; Haider & Levenspiel, 1989). The particle Reynolds number is defined as

$$\mathrm{Re} = \frac{\rho_f w_t d_p}{\mu_f} \tag{3}$$

with μ_f being the fluid viscosity. These correlations, however, are not valid for nonspherical, irregularly shaped particles, for which C_d is a function of both particle Reynolds number and shape. This is a topic of high interest in a wide range of research fields and applications, from industrial (e.g., chemical engineering and hydraulics) to natural processes (sedimentology, volcanology, etc.). In volcanology and Earth sciences in general, the shape-dependent aerodynamic drag is crucial in controlling the transport and deposition of nonspherical solid particles in dust storms (e.g., Doronzo et al., 2015; Kok et al., 2012), rivers and lakes (e.g.,

Table 1
Notation

Symbol	Description	Unit
A_{mp}	Particle maximum projection area	m^2
A_p	Particle surface area	m^2
A_{sph}	Surface area of the equivalent sphere	m^2
C_d	Drag coefficient	-
$C_{d,calc}$	Recalculated drag coefficient	-
$C_{d,meas}$	Measured drag coefficient	-
$C_{d,sphere}$	Drag coefficient of the sphere	-
D_l	Longest particle principal axis	m
D_m	Medium particle principal axis	m
d_p	Particle size	m
D_s	Short particle principal axis	m
d_{sph}	Diameter of the volume equivalent sphere	m
e	Particle elongation	—
f	Particle flatness	—
F_d	Drag force	N
F_N	Newton form factor	—
F_S	Stokes form factor	—
g	Gravitational acceleration	$m\ s^{-2}$
K_N	Newton drag corrector	—
K_S	Stokes drag corrector	—
m	Particle mass	kg
P_c	Perimeter of the circle equivalent to the maximum projection area	m
P_{mp}	Particle maximum projection parameter	m
r	Correlation coefficient	—
Re	Particle Reynolds number	—
RMSE	Root mean squared error	—
v_f	Fluid velocity	$m\ s^{-1}$
v_p	Particle velocity	$m\ s^{-1}$
w_t	Particle terminal velocity	$m\ s^{-1}$
$w_{t,calc}$	Recalculated particle terminal velocity	$m\ s^{-1}$
$w_{t,meas}$	Measured particle terminal velocity	$m\ s^{-1}$
α_2	Function of the particle to fluid density ratio	—
β_2	Function of the particle to fluid density ratio	—
μ_f	Fluid viscosity	Pa s
ε_p	Particle volumetric concentration	—
ρ'	Particle to fluid density ratio	—
ρ_f	Fluid density	$kg\ m^{-3}$
ρ_p	Particle density	$kg\ m^{-3}$
φ	Particle aspect ratio	—
Φ	Particle sphericity	—
ϕ	Particle size in phi units	phi
X	Particle circularity	—
Ψ	Particle shape factor	—

Zhu et al., 2017), pyroclastic flows (e.g., Dellino et al., 2008; Dioguardi & Dellino, 2014), eruptive columns (e.g., Cerminara et al., 2016; Folch et al., 2016), and distal ash clouds (e.g., Beckett et al., 2015; Bonadonna et al., 2012; Bonasia et al., 2010; Costa et al., 2012, 2006). Therefore, a major effort has been posed to find reliable shape-dependent drag laws that work on the widest possible range of fluid dynamic regimes quantified by *Re* (Alfano et al., 2011; Bagheri & Bonadonna, 2016; Chhabra et al., 1999; Chien, 1994; Dellino et al., 2005; Dioguardi et al., 2017; Dioguardi & Mele, 2015; Ganser, 1993; Haider & Levenspiel, 1989; Hölzer & Sommerfeld, 2008; Loth, 2008; Pfeiffer et al., 2005; Swamee & Ojha, 1991; Tran-Cong et al., 2004; Wilson & Huang, 1979). These drag laws are a function of different shape descriptors, among which sphericity Φ is the most widely used. Reviews and discussions on shape descriptors and quantification methods can be found in Bagheri et al. (2015) and Liu et al. (2015). More recently, Dioguardi et al. (2017) showed the potentialities of X-ray microtomographic analyses in this research field and proposed two new drag laws as functions of new tridimensional shape descriptors.

In this work we present a new shape-dependent drag formula, which has been obtained by 304 terminal velocity measurements carried out on 143 volcanic ash and lapilli particles with a wide range of size, density, and shape, falling through fluids of different densities and viscosities. In this law, particle shape is quantified by means of the shape factor Ψ first introduced by Dellino et al. (2005) and later used in Dioguardi et al. (2014) and Dioguardi and Mele (2015). The new drag law has the capability to work in a wide range of fluid dynamic regimes, almost covering all regimes that can be encountered in the aforementioned natural processes, and of particle shapes, from extremely irregular particles to perfect spheres. Results here presented demonstrate an improved performance of predicting the drag of highly irregular particles (like volcanic ash and lapilli) when compared with other drag laws commonly employed in volcanology. The improvement is observed in a very wide *Re* range and especially at the very low *Re*, which is crucial for predicting the fine ash settling from distal ash clouds and plumes.

In the following sections, the shape descriptor and the experiments are briefly recalled, the new drag law is presented, and results from its application are discussed.

2. Particle Shape and Aerodynamic Drag Characterization

2.1. Terminal Velocity Experiments

In order to find the new drag law here presented, we took into account and reviewed the database of experimental measurements presented in Dioguardi and Mele (2015). This database originally included 340 measurements of the aerodynamic drag $C_{d,meas}$ obtained by terminal velocity measurements of 143 irregular solid particles. The samples used came from the volcanic deposits of explosive eruptions at Vesuvius and Campi Flegrei (Italy) (Dellino et al., 2005). The experimental setup consisted of a vertical 1.5 m high glass cylinder with an inner radius of 5 cm. The terminal velocity measurements were carried out in four different fluids: distilled water (ρ_f = 1,000 kg m^{-3}, μ_f = 0.00102 Pa s at 20°C), ethylic alcohol (ρ_f = 810 kg m^{-3}, μ_f = 0.00172 Pa s at 20°C), a solution of glycerin diluted by 13.5% volume of distilled water (ρ_f = 1,235 kg m^{-3}, μ_f = 0.2088 Pa s at 19°C), and another solution of glycerin diluted with 40% of distilled water (ρ_f = 1,172 kg m^{-3}, μ_f = 0.01499 Pa s at 22°C). This allowed us to explore a very wide range of Reynolds number *Re*, from 0.03 to ~10,000. The settling velocity was measured by frame-by-frame tracking of particle fall velocity with a

high-definition video camera (720 × 1,280 pixels) using a recording rate of up to 50 frames s^{-1}. The terminal velocity measurements were repeated for each run, in particular when particles showed secondary movements that could potentially lead to an alteration of the measured terminal velocity due to wall effects.

The original database of Dioguardi and Mele (2015) was revised to ensure the smallest possible error in the determination of settling velocities. As explained in Dioguardi et al. (2017), this error depends on the settling velocity itself and the number of frames considered for calculating the terminal velocity; in particular, the slower the particle, the higher the number of frames (i.e., the time between two particle positions' determinations) necessary for keeping the error within acceptable ranges (~±5%) and vice versa. With this new concept, which was not yet developed and applied in the first version of the database, the number of measurements of the database originally presented in Dioguardi and Mele (2015) was reduced from 340 to 304.

2.2. Particle Shape Characterization

As a shape descriptor, the shape factor Ψ, defined by Dellino et al. (2005), was used. It is the ratio between sphericity Φ and circularity X:

$$\Psi = \frac{\Phi}{X} \tag{4}$$

Sphericity Φ is defined as the ratio of the surface area of the equivalent sphere A_{sph} and the particle surface area A_p, and it quantifies the difference of particle shape from a perfect sphere (for which $\Phi = 1$):

$$\Phi = \frac{A_{\mathrm{sph}}}{A_p} \tag{5}$$

A_{sph} is calculated by means of the diameter of the volume equivalent sphere d_{sph}:

$$d_{\mathrm{sph}} = \sqrt[3]{\frac{6m}{\pi \rho_p}} \tag{6}$$

where m and ρ_p are the mass and density of particle, respectively, which can be determined by the use of a high precision scale and a standard Gay-Lussac picnometer.

Since measuring the particle surface area A_p of irregular particles is not straightforward with image particle analysis technique, this parameter is usually estimated by approximating the particle shape to that of a scalene (or triaxial) ellipsoid:

$$A_p = 4\pi \left(\frac{\left(D_l/2\right)^z \left(D_m/2\right)^z + \left(D_l/2\right)^z \left(D_s/2\right)^z + \left(D_m/2\right)^z \left(D_s/2\right)^z}{3} \right)^{1/z} \tag{7}$$

where D_l, D_m, and D_s are the three principal axes of the particle and $z = 1.6075$ (Dellino et al., 2005).

Circularity, X, is defined as

$$X = \frac{P_{\mathrm{mp}}}{P_c} \tag{8}$$

where P_{mp} and P_c are the maximum projection perimeter and the perimeter of the circle equivalent to the maximum projection area A_{mp} of a particle. Unlike sphericity, circularity is greater than 1, being 1 for a perfect circular contour.

The three perpendicular axes D_l, D_m, and D_s; the maximum projection area A_{mp}, which is the one containing D_l and D_m; and the maximum projection perimeter P_{mp} can be measured by image-analysis techniques on high-resolution digital photographs of particles mounted on a goniometric universal stage. To measure shape parameters of differently sized particles without introducing a scaling error (Dellino & La Volpe, 1996), it is suggested that particle area is in the range 2,500–5,000 pixels, irrespective of the physical particle size. Here a graphical example of calculation is shown on Figure 1 where shape parameters, namely, the three axes, particle area, and particle perimeter, are calculated by means of the free image analysis software ImageJ (https://imagej.nih.gov/ij/). The resulting sphericity, circularity, and shape factor are 0.53, 1.24, and 0.43, respectively.

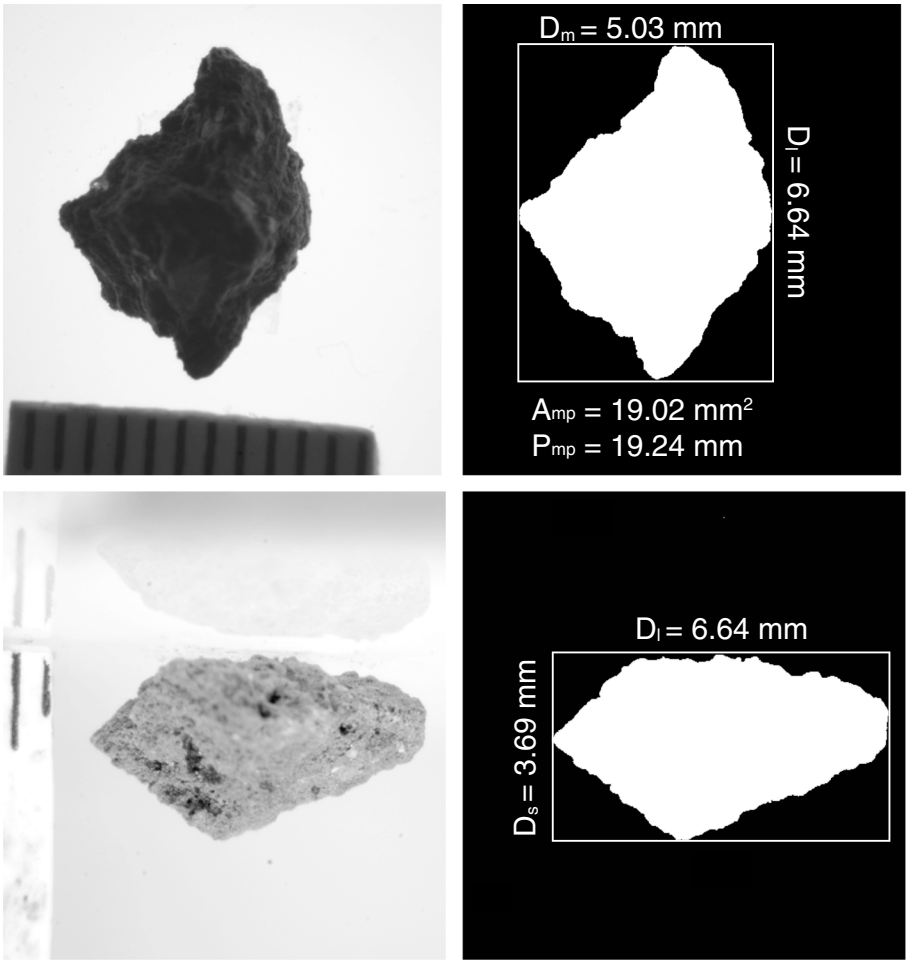

Figure 1. Example of shape parameter (the three main principal axes, particle area, and maximum circle perimeter) determination with image particle analysis carried out with ImageJ on two pictures of particles mounted on a goniometric stage. The first picture above shows the maximum cross section, the second the minimum cross section. *Edited by Daniela Mele (University of Bari). Copyright © 2017.*

Recently employed techniques like X-ray microtomography make it possible to directly estimate A_p and d_{sph}, hence particle sphericity Φ, with the only limitation of the machine resolution (Dioguardi et al., 2017). This technique has the advantage to allow a precise estimation of Φ in particular for medium to fine ash particles, whose mass m (necessary for d_{sph}; see equation (6)) is very difficult to measure and which are very difficult to handle under a microscope for determining the three principal axes. Furthermore, it has the potential to provide a fast estimate of the circularity as well and therefore of the particle shape factor. This will be the object of future investigations. Concerning this work, the shape measurements of the database apply to the above approximation, which is widely employed since it provided robust results, despite the simplification, and it is therefore recommended if it is not possible to employ expensive methods like X-ray microtomography.

All the experimental data and particle parameters are listed in the Excel file "2017JB014926-ds01.xls" available in the supporting information.

3. The New Shape-Dependent Drag Law: Formulation and Results From Intercomparison Analysis

3.1. The New Drag Law

In order to extract the new shape-dependent drag law from our database, we followed an approach different from Dellino et al. (2005) and Dioguardi and Mele (2015), who also presented drag laws as a function of the

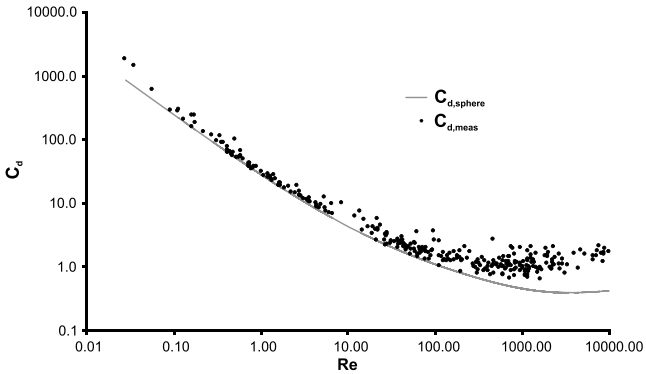

Figure 2. C_d versus *Re* log-log plot showing the measured aerodynamic drag of particles in the database (black dots) $C_{d,\mathrm{meas}}$ and the standard drag curve for a sphere as defined by Haider and Levenspiel (1989) (solid grey line).

shape factor Ψ. Those drag laws were obtained by power law fittings of the experimental data (limited to the experimental *Re* range) and did not ensure the convergence to the drag of a perfect sphere in the limiting case Ψ = 1 over the whole investigated *Re* range. The Dioguardi and Mele law, thanks to the addition of new settling experiments, represented a significant advance in respect to Dellino et al. (2005), in particular for predicting the drag of irregular particles at very low *Re*. However, a stepwise function was introduced that can potentially prevent the calculation from converging to a value of C_d when *Re* was close to the critical value (see section 3.2). The new formulation had therefore to satisfy the following requirements: be valid over the whole investigated *Re* range (~10^{-2} to 10^5), avoid stepwise functions, and be equal to the standard drag curve of spheres in limiting case Ψ = 1.

As the reference law for spheres, the formulation of Haider and Levenspiel (1989) was chosen:

$$C_{d,sphere} = \frac{24}{\mathrm{Re}}\left(1 + 0.1806\,\mathrm{Re}^{0.6459}\right) + \frac{0.4251}{1 + \frac{6880.95}{\mathrm{Re}}} \tag{9}$$

We then analyzed the difference between the measured drag $C_{d,\mathrm{meas}}$ in our database and the drag of a hypothetical sphere $Cd_{,\mathrm{sphere}}$ falling at the same *Re*. Equation (9) can be rearranged into the sum of three parts:

$$C_{d,sphere} = \frac{24}{\mathrm{Re}} + \frac{24}{\mathrm{Re}}\left(0.1806\,\mathrm{Re}^{0.6459}\right) + \frac{0.4251}{1 + \frac{6880.95}{\mathrm{Re}}} \tag{10}$$

It is well known in the literature of multiphase flow physics that the aerodynamic drag of irregular particles is larger than $C_{d,\mathrm{sphere}}$ at any given Reynolds number (Crowe, 2006). This was further verified by our experiments, as can be observed in Figure 2.

The measured drag (black dots) is always higher than $C_{d,\mathrm{sphere}}$ (solid grey line), with a difference that increases as *Re* becomes larger. Some points are, however, very close to the grey line; these points correspond to particles whose shape factor was very close to 1. From these observations we followed the hypothesis about the existence of functions of particle shape that can be applied separately to the three parts of (10) to obtain a fitting law that best interpolates the measured points and allows predicting C_d:

$$C_{d,calc} = \frac{24}{\mathrm{Re}} f_1(\Psi) + \frac{24}{\mathrm{Re}}\left(0.1806\,\mathrm{Re}^{0.6459}\right) f_2(\Psi) + \frac{0.4251}{1 + \frac{6880.95}{\mathrm{Re}}} f_3(\Psi) \tag{11}$$

We then searched for these three functions with the following constraint:

$$f_1(\Psi = 1) = f_2(\Psi = 1) = f_3(\Psi = 1) = 1 \tag{12}$$

as to ensure that the shape-dependent drag law (11) becomes equal to (10) in the limiting case of a spherical particle (Ψ = 1). The three functions were obtained by analyzing the difference between $C_{d,\mathrm{meas}}$ and $C_{d,\mathrm{sphere}}$, focusing on the three parts separately. The assumption has been made that the ratio between each part of $C_{d,\mathrm{sphere}}$ and the total $C_{d,\mathrm{sphere}}$ was equal the ratio between each part of $C_{d,\mathrm{meas}}$ and the total drag for the irregular particles. Thanks to this assumption, f_1, f_2, and f_3 were searched separately by correlating each part of $C_{d,\mathrm{calc}}$ with Ψ and *Re* with the aim at minimizing the error when predicting the experimentally measured terminal velocities $w_{t,\mathrm{meas}}$. It was found that the three functions satisfying the constraints were

$$f_1(\Psi) = \left(\frac{1 - \Psi}{\mathrm{Re}} + 1\right)^{\exp} 1 \tag{13a}$$

$$f_2(\Psi) = \Psi^{-\left(\mathrm{Re}^{\exp} 2\right)} \tag{13b}$$

$$f_3(\Psi) = \Psi^{\exp} 3 \tag{13c}$$

The values of the three exponents exp1, exp2, and exp3 were obtained by iteratively searching for the values that allowed the best fit of the experimental data; this was carried out by means of a Matlab script. The best values of exp1, exp2, and exp3 were found to be 0.25, 0.08, and 5.05, respectively.

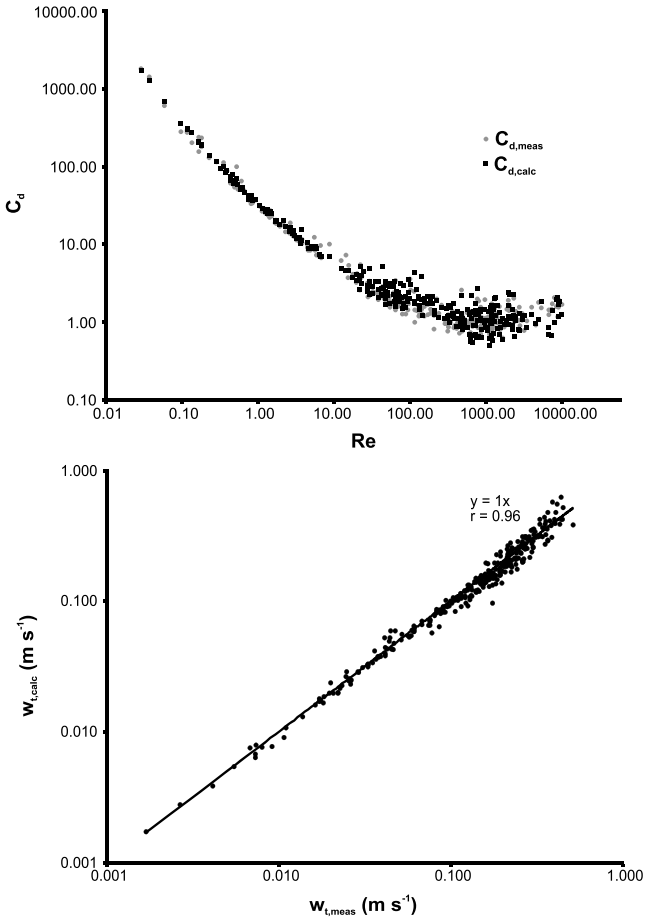

Figure 3. (a) C_d versus *Re* scatter log-log plot comparing the measured aerodynamic drag of particles in the database (grey dots) $C_{d,\mathrm{meas}}$ and the calculated aerodynamic drag of the same particles (black squares) $C_{d,\mathrm{calc}}$ with the new drag law (14). (b) Scatter log-log plot comparing the terminal velocity calculated with the new drag law (14) $w_{t,\mathrm{calc}}$ and the corresponding measured values for the particles in our database, $w_{t,\mathrm{meas}}$. The solid black line is the best fit line of type $y = ax$. The correlation coefficient r is also reported.

Substitution in (11) leads to the new drag formulation:

$$C_{d,calc} = \frac{24}{\mathrm{Re}}\left(\frac{1-\Psi}{\mathrm{Re}}+1\right)^{0.25} + \frac{24}{\mathrm{Re}}\left(0.1806\,\mathrm{Re}^{0.6459}\right)\Psi^{-\left(\mathrm{Re}^{0.08}\right)} + \frac{0.4251}{1+\frac{6880.95}{\mathrm{Re}}\Psi^{-5.05}} \tag{14}$$

Figure 3a shows $C_{d,\mathrm{calc}}$ (black squares) as a function of *Re*, together with $C_{d,\mathrm{meas}}$ (grey dots). A very good agreement can be inferred over the whole investigated range of *Re*. This can be further verified by looking at the scatterplot in Figure 3b, which displays the terminal velocity calculated with (14) $w_{t,\mathrm{calc}}$ versus the measured terminal velocity $w_{t,\mathrm{meas}}$.

Despite some scatter, the quality of the fitting is very good, considering not only the high correlation coefficient (0.96) but also the correlation line, which almost coincides with the perfect equality $y = x$, being the slope 1.001.

Like all the drag laws that explicitly depend on *Re*, an iterative procedure must be employed for calculating C_d, since *Re* depends on w_t, which, in turn, depends on C_d. The iterative procedure consists in the following steps:

Given a guessed value of the particle Reynolds number *Re**, C_d is calculated by equation (14).

From C_d, the terminal velocity w_t can be computed with the Newton's impact law (equation (2)).

With this terminal velocity, a new value of *Re* is calculated (3), and the operations restart from point (1) and are repeated until the difference between the latest updated value of *Re* and that of the previous steps drops within a certain tolerance prescribed by the user. A FORTRAN ("wt_calculator.f90") and a Matlab code ("wt_calculator.m") are available in the supporting information in order to provide the reader with programs that allow direct calculation of the terminal velocity of irregular particles; these pieces of code could be easily implemented in other models like multiphase models and ash dispersion models.

3.2. Comparison With Other Shape-Dependent Drag Laws Commonly Used in Volcanology

In order to quantify the ability of the new drag law to predict the drag and terminal velocity of irregular particles, we compared its performance with that of other laws from the literature whose shape descriptors are available in our database. In particular, the following drag laws were selected: Dellino et al. (2005), Pfeiffer et al. (2005), Ganser (1993), Dioguardi and Mele (2015), and Bagheri and Bonadonna (2016). In the attached supplementary file "2017JB014926-ds01.xls" results from comparisons with other drag laws found in the literature (Chien, 1994; Haider & Levenspiel, 1989; Swamee & Ojha, 1991) are also available in the sheet "Models comparisons." Here we show results from this intercomparison with formulas that are most relevant to volcanology. They are recalled in the following:

Dellino et al. (2005)

$$C_{d,calc} = \frac{0.9297}{\Psi^{1.6}\,\mathrm{Re}^{0.0799}} \tag{15}$$

Pfeiffer et al. (2005): it is a modification of the original law of Walker et al. (1971) and Wilson and Huang (1979).

$$C_{d,calc} = \begin{cases} \frac{24}{\mathrm{Re}}\varphi^{-0.828} + 2\sqrt{1-\varphi} & \mathrm{Re} \le 10^2 \\ 1 - \frac{1 - C_{d,calc}(\mathrm{Re}=100)}{900}\left(10^3 - \mathrm{Re}\right) & 10^2 < \mathrm{Re} \le 10^3 \\ 1 & \mathrm{Re} > 10^3 \end{cases} \tag{16}$$

where $\varphi = (D_m + D_s)/2D_l$ is the particle aspect ratio.

Ganser (1993)

$$C_{d,calc} = \frac{24}{\mathrm{Re}} K_1 K_2 \left[1 + 0.1118 (\mathrm{Re} K_1 K_2)^{0.6567}\right] + \frac{0.4305}{1 + \frac{3305}{\mathrm{Re}} K_1 K_2} \tag{17}$$

where K_1 and K_2 are functions of particle sphericity Φ:

$$K_1 = \left[\frac{1}{3} + \left(\frac{2}{3}\right)\Phi^{-0.5}\right]^{-0.1} \tag{17a}$$

$$K_2 = 10^{1.8148(-\log\Phi)^{0.5743}} \tag{17b}$$

in the case of isometric particles.

Bagheri and Bonadonna (2016)

$$C_{d,calc} = \frac{24 K_s}{\mathrm{Re}} \left[1 + 0.125 \left(\mathrm{Re} \frac{K_N}{K_S}\right)^{2/3}\right] + \frac{0.46 K_N}{1 + \frac{5330}{\mathrm{Re}} \frac{K_N}{K_s}} \tag{18}$$

in which K_s and K_N are complex functions of particle shape and particle to fluid density ratio ρ':

$$K_S = \frac{F_S^{1/3} + F_S^{-1/3}}{2} \tag{18a}$$

$$K_N = 10^{\alpha_2 (-\log F_N)^{\beta_2}} \tag{18b}$$

$$F_S = f e^{1.3} \left(\frac{d_{sph}^3}{D_l D_m D_s}\right) \tag{18c}$$

$$F_N = f^2 e \left(\frac{d_{sph}^3}{D_l D_m D_s}\right) \tag{18d}$$

$$\alpha_2 = 0.45 + \frac{10}{\exp(2.5 \log\rho' + 30)} \tag{18e}$$

$$\beta_2 = 1 - \frac{37}{\exp(3 \log\rho' + 100)} \tag{18f}$$

f and e are the particle flatness and elongation, defined as D_s/D_m and D_m/D_l, respectively.

Dioguardi and Mele (2015)

$$C_{d,calc} = \begin{cases} \frac{C_{d,sphere}}{\mathrm{Re}^2} \Psi^{\mathrm{Re}^{-0.23}} \left(\frac{\mathrm{Re}}{1.1883}\right)^{\frac{1}{0.4826}} & \mathrm{Re} < 50 \\ \frac{C_{d,sphere}}{\mathrm{Re}^2} \Psi^{\mathrm{Re}^{0.05}} \left(\frac{\mathrm{Re}}{1.1883}\right)^{\frac{1}{0.4826}} & \mathrm{Re} > 50 \end{cases} \tag{19}$$

where $C_{d,\mathrm{sphere}}$ was calculated using the drag law of Clift and Gauvin (1971):

$$C_{d,sphere} = \frac{24}{\mathrm{Re}} \left[1 + 0.15\, \mathrm{Re}^{0.687}\right] + \frac{0.42}{1 + \frac{42500}{\mathrm{Re}^{1.16}}} \tag{20}$$

On Figure 4 the drag coefficients calculated with the laws above (black squares) are represented together with $C_{d,\mathrm{meas}}$ (grey dots) in the standard C_d versus Re plot. It is to note that the models' performances are evaluated basing on the specific data set of particle shapes and terminal velocities here presented; consequently, the following considerations are not intended as general statements on the accuracy of the models. Dellino et al. (2005) are not able to reproduce the measured drag coefficients at $Re < 100$; this is not surprising and highlighted by the authors themselves (Dellino et al., 2005, 2012), due to the original database from which the fitting law was extracted, which consisted of drag measurements at $Re > 60$. The drag law performs very well in the fluid dynamic regime for which it was designed, with a good overlap between the calculated and the measured drag coefficients (see plots "Dellino et al. (2005) reduced" in the sheet "Model comparisons" in the attached supplementary "2017JB014926-ds01" Excel file).

The drag law of Pfeiffer et al. (2005) captures the variation of C_d with Re in all the investigated regimes. It underestimates C_d at very low Re and at $Re > 1000$; additionally, in the latter range, it is not able to reproduce the scatter of the measured drag coefficients induced by the shape variation; that is, it neglects the influence

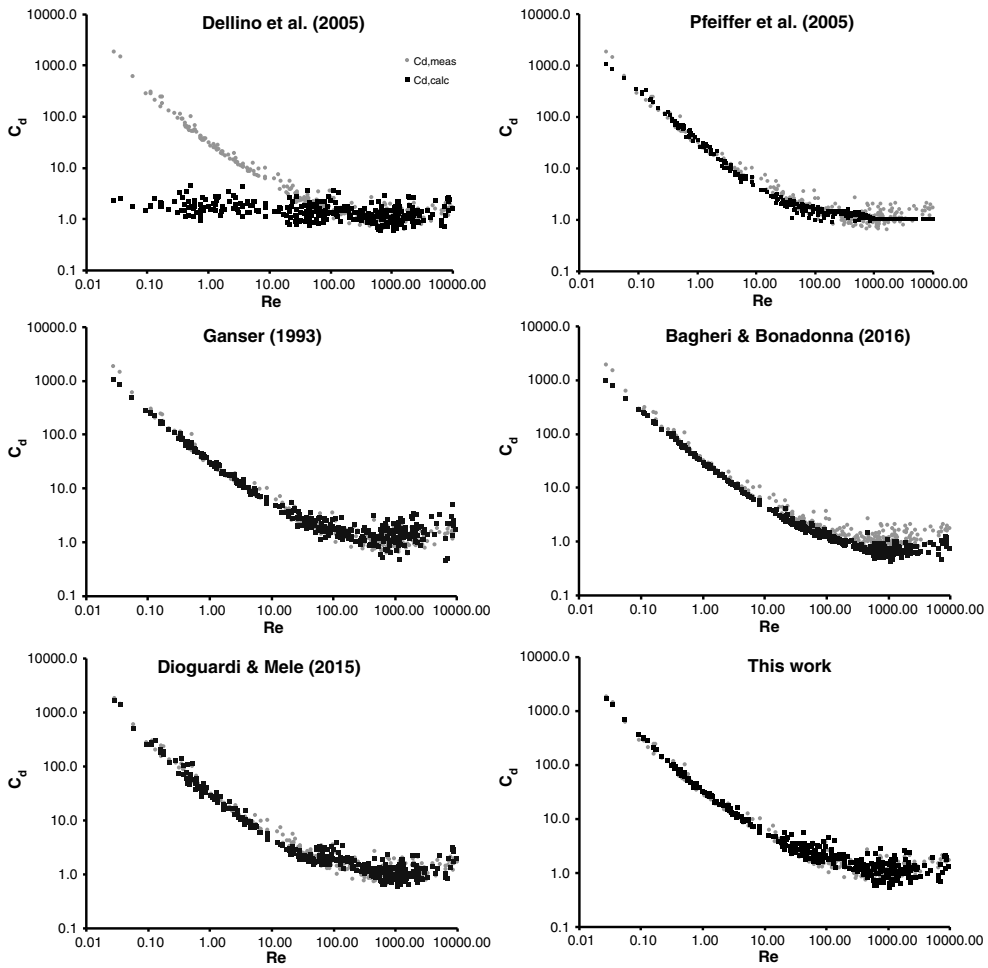

Figure 4. C_d versus *Re* scatter log-log plots comparing the measured aerodynamic drag of particles in the database (grey dots) $C_{d,\mathrm{meas}}$ and the calculated aerodynamic drag of the same particles (black squares) $C_{d,\mathrm{calc}}$ for six selected drag laws: Dellino et al. (2005), Pfeiffer et al. (2005), Ganser (1993), Bagheri and Bonadonna (2016), Dioguardi and Mele (2015), and (14).

of particle shape at high *Re* numbers using the constant drag value of 1 in this range (equation (16)). Much better performance is obtained with Ganser (1993), with an underestimation of $C_{d,\mathrm{meas}}$ at $Re < 0.1$ and an overestimation of the particle shape-induced scatter at high *Re*, together with a tendency to slightly overestimate C_d in this regime. Bagheri and Bonadonna (2016), on the other hand, show a general tendency to underestimate the drag coefficient in the whole *Re* range. This tendency is in particular significant at very low and high *Re*. To insulate the reason of this tendency in such a complex drag law is not straightforward; however, a possible explanation could be that, by definition, the shape parameters in this law (flatness and elongation) do not take into account the small-scale surface irregularities, which play a fundamental role in the case of very irregular volcanic ash and lapilli particles. This is why Dellino et al. (2005) introduced the shape factor Ψ and Dioguardi et al. (2017) used new 3-D shape parameters, all more capable to capture the small-scale surface irregularities. Neglecting surface roughness leads to an underestimation of the drag force, hence of the drag coefficient, which is indeed the general tendency obtained when applying Bagheri and Bonadonna (2016) to our database that is composed of rough volcanic particles only. Dioguardi and Mele (2015) and the new drag law here presented (equation (14)) have the best performance, also at very low *Re*, which proved to be problematic for the other laws but crucial for volcanological applications like ash dispersion modeling. Going deeper into detail, it can be seen that (14) further improved the performance at very low *Re* and in the range 10–100, which is the most problematic for Dioguardi and Mele (2015); this was not surprising, since this range includes the critical value $Re = 50$ at which there is the switch between the two parts of the law (see equation (19)).

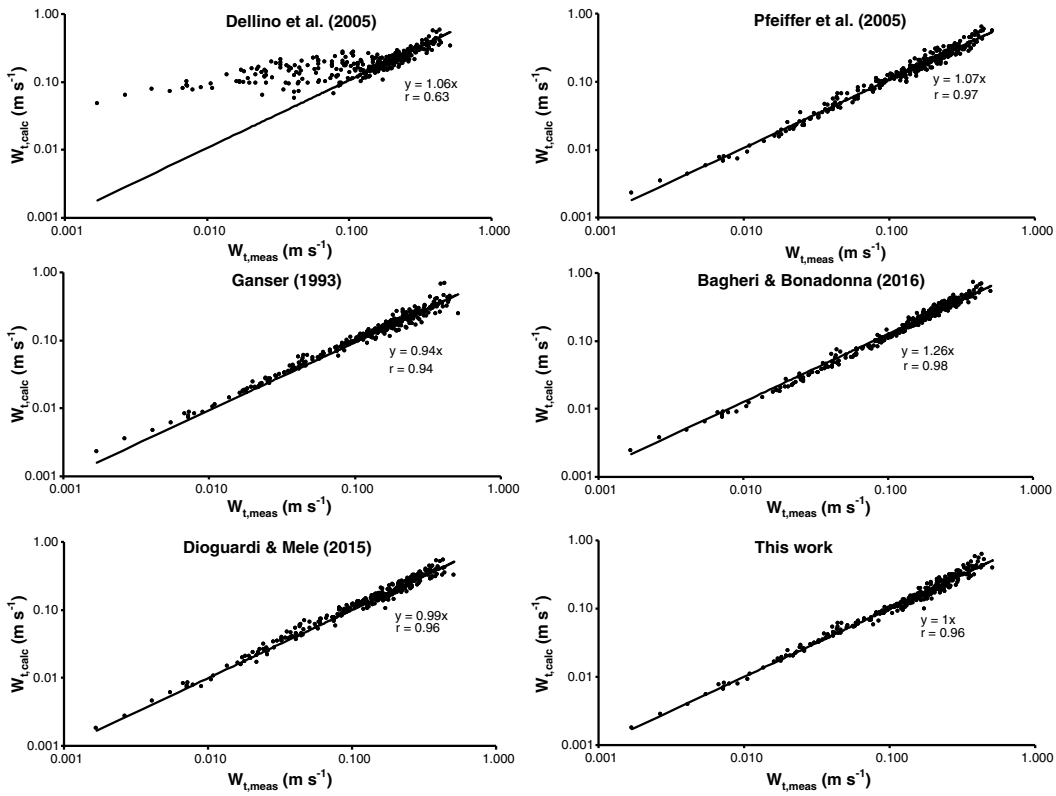

Figure 5. Scatter log-log plots comparing the terminal velocity calculated with six selected drag laws $w_{t,\mathrm{calc}}$ and the corresponding measured values for the particles in our database, $w_{t,\mathrm{meas}}$. The drag laws are Dellino et al. (2005), Pfeiffer et al. (2005), Ganser (1993), Bagheri and Bonadonna (2016), Dioguardi and Mele (2015), and (14). The solid black line is the best fit line of type $y = ax$. The correlation coefficient r is also reported.

In Figure 5 a montage of scatterplots comparing the terminal velocities calculated with the corresponding drag laws ($w_{t,\mathrm{calc}}$) and those measured in the experiments ($w_{t,\mathrm{meas}}$) is presented. The best fit line is also displayed, together with the equation and the correlation coefficient r. Note that the equation is always of a line of the type $\boldsymbol{y} = \boldsymbol{ax}$, since we wanted to judge the performance of the law not only from the value of r but, more importantly, based on the ability to reproduce the measured terminal velocities; the best case would be a very high r with a value of the line slope $\boldsymbol{a} = 1$. The resulting performances reflect those of the recalculation of the drag coefficients. Dellino et al. (2005) have the poorest agreement, with a strong overestimate of the velocities for slow particles. All the other laws apparently have a very similar performance, but a closer inspection reveals important differences. Despite its simplified approach at high *Re*, Pfeiffer et al. (2005) show one of the best performances, with $\boldsymbol{a} = 1.065$, meaning a tendency to slight overestimate terminal velocities. Ganser (1993) shows the opposite, the value of the slope being 0.95, which could be attributed to the tendency to overestimate the drag coefficient (=underestimation of terminal velocity) at very high *Re* that is not counter balanced by the evident tendency to overestimate the terminal velocity at very low *Re*. Bagheri and Bonadonna (2016) had the poorest performance after Dellino et al. (2005), with a value of the slope of 1.261, meaning a general tendency to overestimate terminal velocities, which, in turn, is the result of the drag underestimation in the whole investigated *Re* range. Finally, Dioguardi and Mele (2015) and the new drag law ((14) had the best performances, being a equal to 0.99 and 1, respectively. A closer inspection reveals that the new law better fit the points at terminal velocities between 0.01 and 0.1 m s^{-1} than Dioguardi and Mele (2015).

Table 2
RMSE of Terminal Velocity Recalculation With Different Drag Models

Model	RMSE
Pfeiffer et al. (2005)	16.07%
Ganser (1993)	14.49%
Bagheri and Bonadonna (2016)	24.66%
Dioguardi and Mele (2015)	13.49%
This work (equation (14))	12.76%

These findings are further corroborated by the values of the terminal velocity calculation errors. In particular, we evaluated the

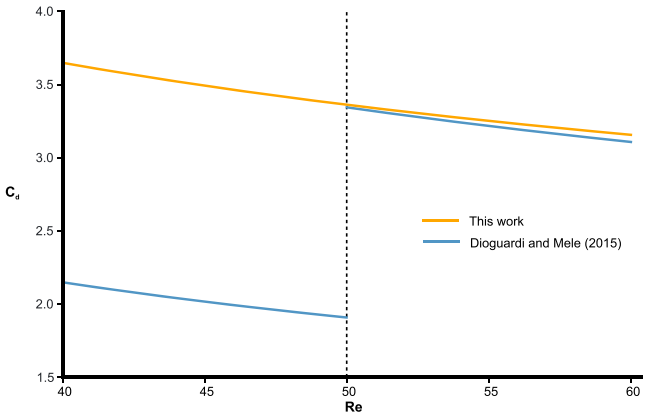

Figure 6. C_d versus *Re* line plot comparing the trend obtained with the new law (14) (solid golden line) and that with Dioguardi and Mele (2015) (solid blue line). The dashed black line represents the limit of the stepwise function of the Dioguardi and Mele formulation, *Re* = 50.

root-mean-square error RMSE for each drag law by applying the following formula:

$$\boldsymbol{RMSE} = \sqrt{\frac{\sum_{i=1}^{N}\left(\frac{w_{t,calc,i}-w_{t,meas,i}}{w_{t,meas,i}}\right)^2 * 100}{N}} \tag{21}$$

where $\boldsymbol{N} = \mathbf{308}$ is the number of terminal velocity measurements in our database (298 in the case of Ganser (1993), since values of sphericity were not available for five particles used in 10 experiments). Table 2 summarizes the results from error analysis.

Here we neglect the RMSE error obtained with Dellino et al. (2005), since the drag law is not valid over the whole *Re* range as already explained. The smallest error is obtained with the new drag law, which slightly improves the performance of the Dioguardi and Mele (2015) law. The highest error is related to the Bagheri and Bonadonna (2016) law. While the improvement in performance of (14) in respect to Dioguardi and Mele (2015) could seem negligible, it has to be stressed that with (14), one can avoid the major drawback of the Dioguardi and Mele law, that is, the stepwise function, together with an additional one linked to the range of applicability that will be discussed in the next section. From several applications of this drag law, in fact, it was observed that in some cases in which *Re* is very close to the critical value of 50, the iterative procedure fails to converge to a specific value of *Re* and C_d.

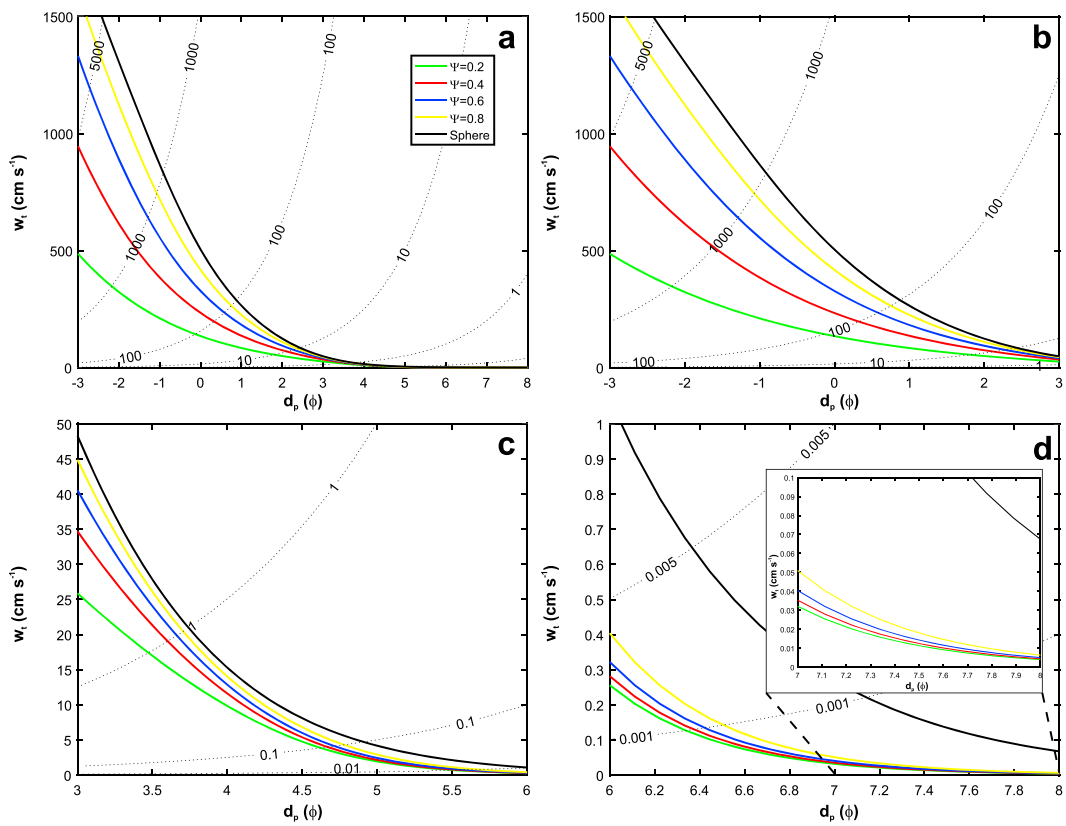

Figure 7. Line plots of particle terminal velocity as a function of grain size for different values of particle shape factor Ψ: Ψ = 0.2: green solid line; Ψ = 0.4: red solid line; Ψ = 0.6: blue solid line; Ψ = 0.8: yellow solid line; Ψ = 1 (sphere): black solid line. The black dotted lines represent constant *Re* values. (a) The complete grain size range (-3ϕ to 8ϕ) is displayed. (b) Focus on grain size range -3ϕ to 3ϕ. (c) Focus on grain size range 3ϕ to 6ϕ. (d) Focus on grain size range 6ϕ to 8ϕ, with a further zoom on the range 7ϕ to 8ϕ.

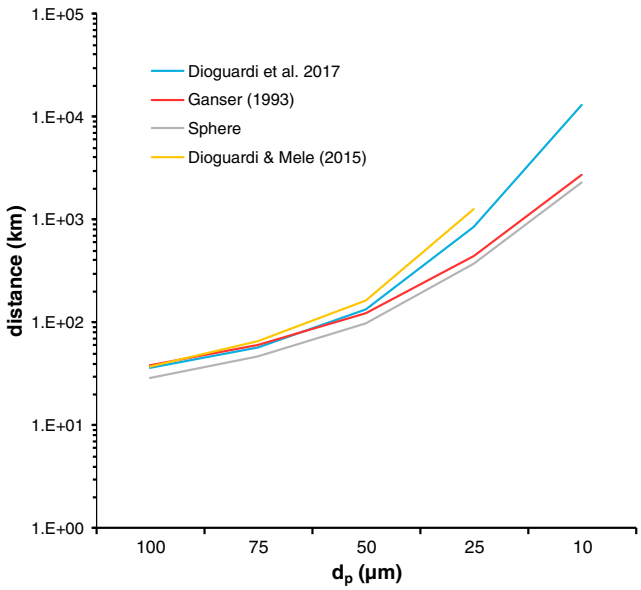

Figure 8. Travelled distances versus particle size (in μm) calculated for a sphere (grey line) and for an irregular particle with shape factor $\Psi = 0.5$ and sphericity $\Phi = 0.6$. The new drag law (blue line), Ganser (1993) (red line), and Dioguardi and Mele (2015) (yellow line) were considered.

Figure 6 presents a line plot of the C_d versus *Re* curve for a particular value of the particle shape factor ($\Psi = 0.5$); the golden line corresponds to Dioguardi and Mele (2015), the blue line to equation (14). The effect of the stepwise function is evident, with a jump of C_d of about 1.5, which is significant at this regimes; in fact, the terminal velocity in air at ground level (ρ_f = 1.2 kg m^{-3}) of a 100 μm-sized particle with a density of 2,500 kg m^{-3} would be in 3.71 m s^{-1} and 2.8 m s^{-1}, if C_d is taken equal to 3.5 and 2, respectively. The new drag law, instead, is a continuous function, hence permitting to avoid any convergence issue and any jump of the calculated C_d values. Also, unlike Dioguardi and Mele (2015), (14) always predicts the drag of a sphere in the limiting case $\Psi = 1$.

Finally, curves of terminal velocities as a function of particle size and shape were traced, in order to verify the capability of the drag law to correctly predict the increase/decrease of terminal velocity as the particle shape factor Ψ increases/decreases. In the line plots of Figure 7, particle size (here presented in ϕ units defined as $\phi = -\log_2 d_p$, where d_p is measured in mm) ranges from -3 to 8ϕ, that is, from coarse lapilli to very fine ash. Five curves are drawn, each one corresponding to a fixed value of particle shape factor (0.2, 0.4, 0.6, 0.8, and 1 for the sphere). The dotted lines are isolines of constant values of *Re*. Figure 7a is the plot with the whole grain size range, and Figures 7b–7d display zooms of restricted size ranges (-3 to 3ϕ, 3 to 6ϕ, and 6 to 8ϕ, respectively).

From inspecting these plots, one can appreciate that the terminal velocity follows the correct expected trend, with decreasing values as the particle size decreases and increasing values as particle shape factor increases. Additionally, the difference of terminal velocity between the curves increases as the particle size/*Re* increases, as expected. Finally, for very fine particles, the influence of shape on terminal velocity decreases until it seems to vanish for very fine ash, but still, there is a difference between irregular and spherical particles.

4. Discussion and Conclusion

We derived a new drag law for irregularly shaped nonspherical particles, based on a series of settling experiments with real volcanic ash and lapilli particles at different fluid dynamic regimes. Our new law was obtained from a database where *Re* ranges from 0.03 to 10,000 and the particle shape factor Ψ from 0.335 to 0.943, thus guaranteeing applicability to a very wide range of fluid dynamic regimes and particle shapes. The new drag law is represented by a single equation, hence circumventing the need of a stepwise equation when modeling the terminal velocity of solid particulate material. It is a function of the particle shape factor Ψ, a shape parameter that proved to be a robust descriptor of the irregular shape of volcanic particles and that can be measured by means of the most commonly used image particle analysis techniques and more recent X-ray microtomography analyses. We acknowledge that measuring Ψ is not always straightforward and that more data of sphericity Φ are available in the literature. For this reason, a first-order approximate relationship (see sheet "Shape comparison" in supporting information Data Set S1)

$$\boldsymbol{\Psi = 0.83\Phi} \tag{22}$$

The regression line has a correlation factor *r* of 0.83 due to some scatter between the points; however, it is significantly different from 0, that is, the case of no correlation, as results from the Student *t* test carried out on *r* (see supporting information). Furthermore, an analysis of variance on the correlation law was conducted and further confirms that the model (22) provides a significantly good approximation of Ψ if Φ is available (and vice versa).

We evaluated the performance of the new drag law when recalculating the experimentally measured terminal velocities and compared it with that of other shape-dependent drag laws selected from the multiphase fluid dynamics and volcanological literature, based on the availability of the shape descriptors used in these laws in our database. Focusing on the drag laws developed and used in volcanology, the performance of the

new drag law is significantly improved for the presented database, in particular at very low *Re*, a fluid dynamic regime that is of interest for applications like the fine ash dispersion and settling modeling. Furthermore, results show that the effect of particle shape cannot be neglected even at very low *Re*, which, in volcanological processes, translates to very small particles. This has important implications for the simulation of the distal ash dispersal, meaning that the use of realistic values of the shape parameters is recommended also in such applications. As a further verification, the distances travelled by hypothetical particles falling from 20 km height in a uniform cross wind of 10 m s^{-1} were calculated. This was achieved by calculating the particle terminal velocity (the new drag law (14), Ganser (1993) (17), and Dioguardi and Mele (2015) (19) were selected) and, subsequently, the falling time; the distance travelled was then estimated by assuming that the particle was fully coupled to the horizontal cross-flow, hence by multiplying the falling time by the wind speed. For simplicity, air density and viscosity were assumed to be constant and equal to the height-averaged values over the first 20 km from sea level of the International Standard Atmosphere, that is, 0.47 kg m^{-3} and 1.54 Pa s, respectively. Particle density and shape factor were set to 2,500 kg m^{-3} and 0.5, respectively. Particle sphericity needed for using (17) was set to 0.6, as estimated by means of (22). The case of a perfect sphere was also considered, with the aerodynamic drag calculated by the model of Haider and Levenspiel (1989) (equation (9)). Different values of particle size d_p were considered: 10, 25, 50, 75, and 100 μm. Results of this exercise are shown in Figure 8.

All the models predict an increasing distance as particle size decreases. Excluding the case of a perfect sphere, there are no significant differences when $d_p > 75$ μm, as was expected in this fluid dynamic regime ($0.5 < Re < 2$) where these drag laws showed very similar performances (see Figure 4). For a 50 μm particle, the distances start to become significantly different, especially Dioguardi and Mele (2015), which predict the lowest terminal velocity, hence the largest distance. The differences increase as particle size decreases, becoming very important at d_p = 10 μm between the new drag law (14) and that of Ganser (17) (~8,000 km). It is to note that the drag law of Dioguardi and Mele (2015) failed to converge for this grain size at very low *Re* (<0.001), not surprisingly since this empirical drag law was designed to work in the range $0.01 < Re < 10{,}000$. These differences, though obtained from a highly simplified test case, demonstrate that, at very low Reynolds numbers, the apparently small differences in performance between the different drag laws translate into significant difference when computing the distance travelled by very fine particles in the atmosphere. The relevance of these findings for ash dispersion modeling is evident and justifies additional research aimed both at further populating the volcanological databases of drag measurements of volcanic particles at very low Reynolds numbers and quantifying the shape parameters of fine ash particles.

Thanks to its wide range of applicability both considering the fluid dynamic regime and the particle shape irregularity, the new drag law can be applied to any kind of multiphase flow modeling of the transport of solid irregular particles in a Eulerian-Lagrangian fashion. In particular, the new drag law can be applied to different volcanological processes, spanning from the simulation of particles settling from volcanic plumes and distal clouds in plume and ash dispersion models to the transport of volcanic ash and lapilli in particle-laden gravity flows (e.g., pyroclastic density currents). The next steps include the compilation of a unified database of particle shape and drag measurements that can be made available to the multiphase flow and volcanological community and the upscaling of the new knowledge gained on the drag of single irregular particle to mixture of particles, a step that is important for multiphase flow modeling at large scale and significant solid particle concentrations.

Acknowledgments
Published with permission of the Executive Director of British Geological Survey (NERC). We thank Larry Mastin and an anonymous reviewer for their very useful suggestion that helped to significantly improve the manuscript. Supporting data can be retrieved from the following link: https://bgs.sharefile.eu/d-sb0c45951cfd470c9.

References

Alfano, F., Bonadonna, C., Delmelle, P., & Costantini, L. (2011). Insights on tephra settling velocity from morphological observations. *Journal of Volcanology and Geothermal Research*, *208*(3–4), 86–98. https://doi.org/10.1016/j.jvolgeores.2011.09.013

Bagheri, G., & Bonadonna, C. (2016). On the drag of freely falling non-spherical particles. *Powder Technology*, *301*, 526–544. https://doi.org/10.1016/j.powtec.2016.06.015

Bagheri, G., Bonadonna, C., Manzella, I., & Vonlanthen, P. (2015). On the characterization of size and shape of irregular particles. *Powder Technology*, *270*, 141–153. https://doi.org/10.1016/j.powtec.2014.10.015

Beckett, F. M., Witham, C. S., Hort, M. C., Stevenson, J. A., Bonadonna, C., & Millington, S. C. (2015). Sensitivity of dispersion model forecasts of volcanic ash clouds to the physical characteristics of the particles. *Journal of Geophysical Research: Atmospheres*, *120*, 11,636–11,652. https://doi.org/10.1002/2015JD023609

Bonadonna, C., Folch, A., Loughling, S., & Puempel, H. (2012). Future developments in modelling and monitoring of volcanic ash clouds: Outcomes from the first IAVCEI-WMO workshop on Ash Dispersal Forecast and Civil Aviation. *Bulletin of Volcanology*, *74*, 1–10. https://doi.org/10.1007/s00445-011-0508-6

Bonasia, R., Macedonio, G., Costa, A., Mele, D., & Sulpizio, R. (2010). Numerical inversion and analysis of tephra fallout deposits from the 472 AD sub-Plinian eruption at Vesuvius (Italy) through a new best-fit procedure. *Journal of Volcanology and Geothermal Research*, *189*, 238–246. https://doi.org/10.1016/j.jvolgeores.2009.11.009

Cerminara, M., Esposti Ongaro, T., & Berselli, L. C. (2016). ASHEE-1.0: A compressible, equilibrium-Eulerian model for volcanic ash plumes. *Geoscientific Model Development*, *9*, 697–730. https://doi.org/10.5194/gmd-9-697-2016

Chhabra, R. P., Agarwal, L., & Sinha, N. K. (1999). Drag on non-spherical particles: An evaluation of available methods. *Powder Technology*, *101*, 288–295.

Chien, S. F. (1994). Settling velocity of irregularly shaped particles. *SPE Drilling and Completion*, *9*, 281–288.

Clift, R., & Gauvin, W. H. (1971). Motion of entrained particles in gas stream. *Canadian Journal of Chemical Engineering*, *49*(4), 439–448.

Costa, A., Macedonio, G., & Folch, A. (2006). A three-dimensional Eulerian model for transport and deposition of volcanic ashes. *Earth and Planetary Science Letters*, *241*, 634–647.

Costa, A., Folch, A., Macedonio, G., Giaccio, B., Isaia, R., & Smith, V. (2012). Quantifying volcanic ash dispersal and impact from Campanian Ignimbrite super-eruption. *Geophysical Research Letters*, *39*, L10310. https://doi.org/10.1029/2012GL051605

Crowe, C. T. (2006). *Multiphase flow handbook*. Boca Raton, FL: Taylor & Francis.

Dellino, P., Gudmundsson, M. T., Larsen, G., Mele, D., Stevenson, J. A., Thordarson, T., & Zimanowski, B. (2012). Ash from the Eyjafjallajökull eruption (Iceland): Fragmentation processes and aerodynamic behavior. *Journal of Geophysical Research*, *117*, B00C04. https://doi.org/10.1029/2011JB008726

Dellino, P., & La Volpe, L. (1996). Image processing analysis in reconstructing fragmentation and transportation mechanisms of pyroclastic deposits. The case of Monte Pilato-Rocche Rosse eruptions, Lipari (Aeolian Islands, Italy). *Journal of Volcanology and Geothermal Research*, *71*, 13–29. https://doi.org/10.1016/0377-0273(95)00062-3

Dellino, P., Mele, D., Bonasia, R., Braia, G., La Volpe, L., & Sulpizio, R. (2005). The analysis of the influence of pumice shape on its terminal velocity. *Geophysical Research Letters*, *32*, L21306. https://doi.org/10.1029/2005GL023954

Dellino, P., Mele, D., Sulpizio, R., La Volpe, L., & Braia, G. (2008). A method for the calculation of the impact parameters of dilute pyroclastic density currents based on deposit particle characteristics. *Journal of Geophysical Research*, *113*, B07206. https://doi.org/10.1029/2007B005365

Dioguardi, F., & Dellino, P. (2014). PYFLOW: A computer code for the calculation of the impact parameters of dilute pyroclastic density currents (DPDC) based on field data. *Computational Geosciences*, *66*, 200–210. https://doi.org/10.1016/j.cageo.2014.01.013

Dioguardi, F., & Mele, D. (2015). A new shape dependent drag correlation formula for non-spherical rough particles. Experiments and results. *Powder Technology*, *277*, 222–230. https://doi.org/10.1016/j.powtec.2015.02.062

Dioguardi, F., Dellino, P., & Mele, D. (2014). Integration of a new shape-dependent particle-fluid drag coefficient law in the multiphase Eulerian-Lagrangian code MFIX-DEM. *Powder Technology*, *260*, 68–77. https://doi.org/10.1016/j.powtec.2014.03.071

Dioguardi, F., Mele, D., Dellino, P., & Dürig, T. (2017). The terminal velocity of volcanic particles with shape obtained from 3D X-ray micro-tomography. *Journal of Volcanology and Geothermal Research*, *329*, 41–53. https://doi.org/10.1016/j.jvolgeores.2016.11.013

Doronzo, D. M., Khalaf, E. A., Dellino, P., de Tullio, M. D., Dioguardi, F., Gurioli, L., … Sulpizio, R. (2015). Local impact of dust storms around a suburban building in arid and semi-arid regions: Numerical simulation examples from Dubai and Riyadh, Arabian Peninsula. *Arabian Journal of Geosciences*, *8*(9), 7359–7369. https://doi.org/10.1007/s12517-014-1730-2

Folch, A., Costa, A., & Macedonio, G. (2016). FPLUME-1.0: An integral volcanic plume model accounting for ash aggregation. *Geoscientific Model Development*, *9*, 431–450. https://doi.org/10.5194/gmd-9-431-2016

Ganser, G. (1993). A rational approach to drag prediction of spherical and nonspherical particles. *Powder Technology*, *77*, 143–152.

Haider, A., & Levenspiel, O. (1989). Drag coefficient and terminal velocity of spherical and nonspherical particles. *Powder Technology*, *58*, 63–70. https://doi.org/10.1016/00325910(89)80008-7

Hölzer, A., & Sommerfeld, M. (2008). New simple correlation formula for the drag coefficient of non-spherical particles. *Powder Technology*, *184*, 361–365. https://doi.org/10.1016/j.powtec.2007.08.021

Kok, J. F., Parteli, E. J. R., Michaels, T. I., & Karam, D. B. (2012). The physics of wind blown sand and dust. *Reports on Progress in Physics*, *75*, 1–72.

Liu, E. J., Cashman, K. V., & Rust, A. (2015). Optimising shape analysis to quantify volcanic ash morphology. *GeoResJ*, *8*, 14–30. https://doi.org/10.1016/j.grj.2015.09.001

Loth, E. (2008). Drag of non-spherical solid particles of regular and irregular shape. *Powder Technology*, *182*, 342–353. https://doi.org/10.1016/j.powtec.2007.06.001

Pfeiffer, R., Costa, A., & Macedonio, G. (2005). A model for the numerical simulation of tephra fall deposits. *Journal of Volcanology and Geothermal Research*, *140*, 273–294.

Swamee, P. K., & Ojha, C. P. (1991). Drag coefficient and fall velocity of nonspherical particles. *Journal of Hydraulic Engineering*, *117*, 660–669. https://doi.org/10.1061/(ASCE)0733-9429(1991)117:5(660)

Tran-Cong, S., Gay, M., & Michaelides, E. E. (2004). Drag coefficients of irregularly shaped particles. *Powder Technology*, *139*, 21–32. https://doi.org/10.1016/j.powtec.2003.10.002

Walker, G., Wilson, L., & Bowell, E. (1971). Explosive volcanic eruptions I. Rate of fall of pyroclasts. *Geophysical Journal of the Royal Astronomical Society*, *22*, 377–383.

Wilson, L., & Huang, T. (1979). The influence of shape on the atmospheric settling velocity of volcanic ash particles. *Earth and Planetary Science Letters*, *44*, 311–324.

Zhu, X., Zeng, Y. H., & Huai, W. X. (2017). Settling velocity of non-spherical hydrochorous seeds. *Advances in Water Resources*, *103*, 99–107. https://doi.org/10.1016/j.advwatres.2017.03.001